Journal of the Ceramic Society of Japan 131 [7] 242-247 2023
DOI https://doi.org/10.2109/jcersj2.23002

JCS-Japan

FULL PAPER

In-plane lattice orientation in aluminum scandium nitride epitaxial films deposited on Nb-doped $SrTiO_3(111)$ substrates via reactive magnetron sputtering

Kota Hasegawa[1,2], **Takao Shimizu**[2,3,†] and **Naoki Ohashi**[1,2,4]

[1] Interdisciplinary Graduate School of Engineering Sciences, Kyushu University,
6–1 Kasuga-koen, Kasuga, Fukuoka 816–8580, Japan
[2] National Institute for Materials Science, 1–1 Namiki, Tsukuba, Ibaraki 305–0044, Japan
[3] JST-PRESTO, Japan Science and Technology Agency, 4–1–8 Honcho, Kawaguchi, Saitama 332–0012, Japan
[4] MDX Research Center for Element Strategy, Tokyo Institute of Technology, 4259 Nagatsuta, Midori-ku, Yokohama 226–8503, Japan

Wurtzite-type aluminum scandium nitride [WZ-$(Al_{1-x}Sc_x)N$] thin films were grown on 0.5 wt % Nb-doped $SrTiO_3(111)$ (Nb:STO) single crystal substrates using the radio frequency reactive magnetron sputtering method with Al and Sc targets. WZ-$(Al_{1-x}Sc_x)N$ thin films with $0 \le x \le 0.49$ were epitaxially grown on Nb:STO substrates. Films with $x \le 0.3$ exhibited multi-domain *in-plane* orientation. The coexistence of two rotation domains, (Al,Sc)N[100]//Nb:STO$[1\bar{1}0]$ and (Al,Sc)N[100]//Nb:STO$[11\bar{2}]$, was observed. The abundance of these two domains varied with x, and films with $x > 0.3$ were single-crystal-like single-domain films. Although the lattice parameters and domain structure intricately changed with x, the calculated unit cell volume was in accordance with the Vegard's law. These results indicate that the unit cell volume is determined by the chemical composition.

Key-words : (Al,Sc)N, $SrTiO_3(111)$, Reactive magnetron sputtering, Epitaxial films

[Received January 7, 2023; Accepted April 19, 2023]

1. Introduction

Wurtzite-type aluminum nitride, which possesses a wide bandgap, high dielectric strength, high thermal conductivity, and low acoustic and dielectric losses, has been extensively developed for applications in optoelectronics,1) electric insulation substrates,2) and microelectromechanical system (MEMS) filters.3) Solid-solution compounds, such as (Al,Ga)N, have also attracted significant attention in power electronics and ultraviolet lighting devices because of their potential for bandgap engineering.4) This study focuses on wurtzite-type solid-solution systems of aluminum scandium nitride [WZ-$(Al_{1-x}Sc_x)N$]. This solid-solution system has significant potential for MEMS applications because its electromechanical performance can be enhanced by substituting Al with Sc.5),6) WZ-$(Al_{1-x}Sc_x)N$ is also known as the first ferroelectric wurtzite-type crystal; Fichtner et al. observed polarity switching in WZ-$(Al_{1-x}Sc_x)N$ in 2019.7) Before their discovery, WZ-type compounds were regarded as pyroelectric materials but not ferroelectric materials. The ferroelectric behavior of WZ-$(Al_{1-x}Sc_x)N$ is different from that of other conventional ferroelectric compounds, e.g., significantly high spontaneous polarization (80–110 $\mu C/cm^2$) and a high coercive field (1.8–5 MV/cm).

The metal/dielectric/metal (MIM) structure is the most fundamental structure used in dielectric and piezoelectric devices. For instance, a Pt-based MIM, Pt/oxide/Pt, is a widely employed conventional structure for characterizing dielectric and piezoelectric materials. Note that the bottom electrodes act as an electric contact to introduce the electric field and electric current and as a structural template to deposit the insulator layer. As the crystallinity of the insulator layer depends on the interfacial structure between the bottom electrode and the dielectric layer, the structure and chemical composition of the bottom electrode layer are key factors in the synthesis of high-quality insulator layers in MIM structures. Significant research has been conducted on the effects of the bottom electrodes on the properties and structures of ferroelectrics, aiming to improve the ferroelectricity of titanates for the development of MIM structures.8)–10) The selection of the bottom electrode layer used in MIM structures involving WZ-$(Al_{1-x}Sc_x)N$ thin-film insulator layers is important. For instance, Nie et al. reported that MIM structures with highly *c*-axis-aligned WZ-$(Al_{1-x}Sc_x)N$ films, obtained using a platinum bottom electrode, possessed a high breakdown field strength and

---

[†] Corresponding author: T. Shimizu; E-mail: SHIMIZU.Takao@nims.go.jp

[‡] Preface for this article: DOI https://doi.org/10.2109/jcersj2.131.P7-1

low leakage current compared to those obtained using a molybdenum electrode.[11]

The selection of the bottom electrode is essential for the high performance of MIM structure devices. Here, the importance of the *in-plane* lattice parameters must be emphasized. In our previous study, we investigated the effect of the lattice parameters of stressed AlN on its ferroelectric properties.[12] The ratio of *c*- and *a*-axis lengths (c/a) is an essential parameter for determining ferroelectric switching behavior in WZ-($Al_{1-x}Sc_x$)N, based on the ferroelectric switching mechanism proposed by Moriwake et al.[13] We hypothesized that both the *out-of-plane* (*c*-axis) and *in-plane* (*a*-axis) lattice parameters should be considered when investigating ferroelectricity in WZ-($Al_{1-x}Sc_x$)N. Yazawa et al. reported that the coercive field of WZ-($Al_{1-x}Sc_x$)N varies with its *c*-axis length,[14] attributing the variation in the *c*-axis length to structural constraints at the film/electrode interfaces. In order to study *in-plane* lattice parameters as well as electric properties of dielectric layers, usage of highly conductive single crystal substrate appropriate to obtain epitaxial layer is the most conventional way. Hence, in this study, a heavily Nb-doped $SrTiO_3$ single crystal with a very low electrical resistivity of 0.001 (Ω·cm) was used to study the crystal structure of WZ-($Al_{1-x}Sc_x$)N films.

Several reports have been published on the epitaxial growth of WZ-AlN on a $SrTiO_3$(111) single-crystal substrates using molecular beam epitaxy,[15] pulsed laser deposition,[16] and magnetron sputtering.[17],[18] Although $SrTiO_3$ has a cubic rather than a hexagonal lattice, three-fold symmetry exists along the $\langle 111 \rangle$ axis, and the oxygen sublattice is considered suitable for the epitaxial growth of films with hexagonal symmetry. The epitaxial growth of ZnO, which has a WZ-type structure, was achieved using the (111) face of a cubic lattice.[19] This finding motivated us to study the epitaxial growth of WZ-($Al_{1-x}Sc_x$)N on Nb:STO(111) single-crystal substrates. Previous studies on WZ-AlN on $SrTiO_3$(111) revealed changes in the domain structure with increasing deposition temperature. Ferroelectric properties, particularly switching dynamics, are strongly affected by the domain structure. Therefore, investigating the *in-plane* epitaxial relationship and domain structure of WZ-($Al_{1-x}Sc_x$)N on Nb:STO(111) single-crystal substrates is of considerable significance.[20],[21]

In this study, we successfully deposited epitaxial WZ-($Al_{1-x}Sc_x$)N thin films with $0 \le x < 0.5$, which are appropriate for studying the relationships between the crystal structure and chemical composition (x), on Nb:STO(111) single-crystal substrates using radio frequency (RF) reactive magnetron sputtering. We also discuss the *in-plane* rotation domains of the WZ-($Al_{1-x}Sc_x$)N films and the *in-plane* lattice parameters.

2. Experimental methods

($Al_{1-x}Sc_x$)N thin films were deposited on Nb:STO(111) single-crystal substrates via RF reactive magnetron sputtering. Commercially available single crystals with 0.5 wt % Nb and an electron concentration above 2.0×10^{20} cm^{-3} at room temperature were used.[22] The error of orientation was estimated as ±0.1°. The substrate was heated to 450 °C and rotated during the deposition. The chamber pressure was maintained at 0.7 Pa by introducing high-purity argon (99.999 %) and nitrogen (99.999 %) gases at a ratio of 1:1. The background pressure in the deposition chamber was maintained below 2.0×10^{-6} Pa to avoid the unintentional oxidation of the films and targets. Solid-solution films were deposited via co-sputtering using an independently controlled dual-cathode source of pure aluminum (99.999 %) and scandium (99.99 %). The composition x in ($Al_{1-x}Sc_x$)N was controlled by changing the RF power from 45 to 100 W for the aluminum source and from 0 to 55 W for the scandium source. Before deposition, pre-sputtering was performed under deposition conditions for over 30 min to stabilize the discharge and remove surface contamination on each target.

The film thickness and composition were determined via X-ray fluorescence spectroscopy using a ZSX Primus spectrometer (Rigaku Co., Ltd., Tokyo, Japan). The crystal structures of the ($Al_{1-x}Sc_x$)N thin films were investigated via X-ray diffraction (XRD) using a SmartLab diffractometer (Rigaku Co., Ltd., Tokyo, Japan) with Cu-Kα radiation. Phase identification and the determination of the *out-of-plane* lattice parameters were performed using conventional θ–2θ mode scans. Additionally, ϕ-scan measurements using the (101) diffraction of WZ-($Al_{1-x}Sc_x$)N were performed to determine the epitaxial relationship between the crystalline lattices of the films and substrates. Furthermore, ω–2θ mode scans were performed to evaluate the *d*-spacing corresponding to the (101) diffraction of WZ-($Al_{1-x}Sc_x$)N and to deduce the *in-plane* lattice parameters.

3. Results and discussion

The deposition conditions and the characteristics of the resulting films are summarized in **Table 1**. The film thickness and composition are shown as functions of the RF input power during the deposition. The cation composition x in the deposited films was highly dependent on the input power and was successfully controlled in the range of $0 \le x \le 0.49$. Reproducibility of the film composition was confirmed by repeating the experiment for several times under the same deposition conditions.

Figure 1 shows the XRD θ–2θ patterns of the ($Al_{1-x}Sc_x$)N samples. Only the diffraction peak assignable to the 00l diffraction of WZ-($Al_{1-x}Sc_x$)N was observed in the diffraction pattern with 111 diffraction peak from

Table 1. Sample specifications, RF power conditions, and thickness and composition of ($Al_{1-x}Sc_x$)N thin films

Sample	RF power for Al (W)	RF power for Sc (W)	Thickness (nm)	x in ($Al_{1-x}Sc_x$)N
(a)	100	0	150	0
(b)	74	26	128	0.09
(c)	70	30	128	0.18
(d)	60	40	124	0.30
(e)	53	47	111	0.37
(f)	45	55	109	0.49

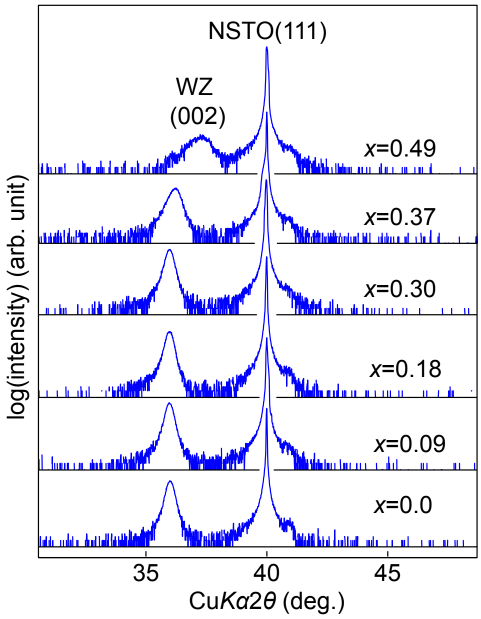

Fig. 1. XRD θ–2θ patterns for $(Al_{1-x}Sc_x)N$ thin films with $0 \le x < 0.5$, measured at room temperature. 'WZ(002)' and 'NSTO(111)' denote the 002 diffraction peak of WZ-$(Al_{1-x}Sc_x)N$ and 111 diffraction peak of Nb-doped $SrTiO_3$, respectively.

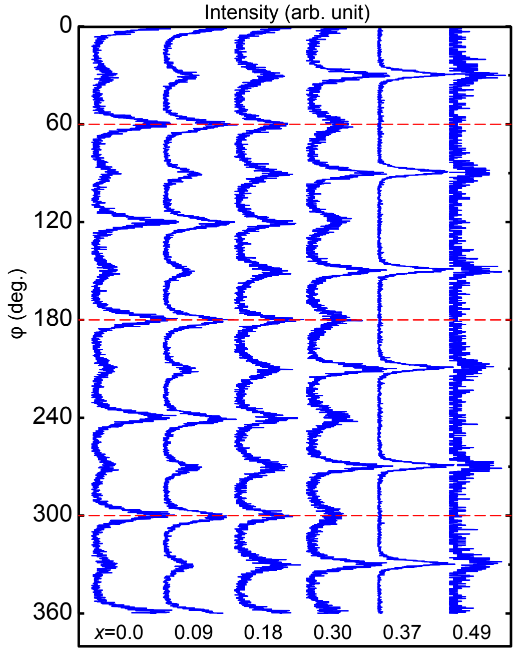

Fig. 2. XRD φ scans of the 101 diffraction of WZ-$(Al_{1-x}Sc_x)N$ ($0 \le x < 0.5$). Dashed lines indicate the projection of the $\langle 100 \rangle$ direction of the Nb-doped $SrTiO_3$ substrate.

Nb:STO. The 002 peak of WZ-$(Al_{1-x}Sc_x)N$ is observed at approximately 36.01° for $x \le 0.37$. For $x = 0.49$, the peak attributed to this diffraction was observed at a higher diffraction angle, indicating a decrease in the lattice parameter. The peak at 36.01° for the film with $x = 0$ corresponds to the 002 diffraction peak of bulk AlN ($c = 4.980$ Å) generally detected at 36.04°.[23] Our results also indicate that the c-axis lattice parameter of WZ-$(Al_{1-x}Sc_x)N$ is not sensitive to the chemical composition x for $x \le 0.37$. Based on the table of ionic radii,[24] Sc^{3+} ions are significantly larger than Al^{3+} ions. Although the ionic radius of Sc^{3+} at four-fold coordination sites is not listed in the table, Sc^{3+} is substantially larger than Al^{3+} when comparing the ionic radii at six-fold coordination sites. Therefore, the lattice should expand with an increase in x. However, the c-lattice parameter did not change significantly with x for $x \le 0.37$. Considering the ionic radii of Sc^{3+} and Al^{3+}, the reduction in the lattice parameter for $x = 0.49$ is notable. The abrupt change in the peak position give rise to suspicion that the WZ structure could not be maintained at this composition or that Sc is not sufficiently solved. The evaluation of the *in-plane* (a-axis) lattice parameter is important for confirming the formation of solid-solution WZ-$(Al_{1-x}Sc_x)N$ for the full range of x and determining its crystal structure.

Figure 2 shows the XRD ϕ scans of the 101 diffraction of WZ-$(Al_{1-x}Sc_x)N$. The dashed red lines in the figure correspond to the projection of the $\langle 001 \rangle$ axis of the Nb:STO substrate. The $(Al_{1-x}Sc_x)N$ samples with $0 \le x \le 0.3$ showed 12 peaks separated by 30°. However, only six peaks should have been detected in the ϕ-scan because of the six-fold symmetry of the WZ structure. These results indicate the presence of *in-plane* rotation domains. The WZ-$(Al_{1-x}Sc_x)N$ samples with $0.3 < x < 0.5$ showed six peaks separated by 60°, suggesting that WZ-$(Al_{1-x}Sc_x)N$ is well aligned to form a single-crystal-like structure. For samples with $x \le 0.3$, the epitaxial relationships are expressed as WZ-(Al,Sc)N[100]//Nb:STO[$11\bar{2}$] for one domain and WZ-(Al,Sc)N[100]//Nb:STO[$1\bar{1}0$] for the other domain, as illustrated in **Fig. 3**. The triangles represent the size of the oxygen sublattice at the (111) face of Nb:STO, and the hexagons represent the nitrogen sublattice in WZ-type nitrides. We expect that the interfacial structures of AlN and Nb:STO will match as shown in Fig. 3(B), considering that the size of the oxygen sublattice on the Nb:STO(111) face and the nitrogen sublattice at the (001) face of AlN should lead to good lattice matching. However, our results suggest that the structure of the AlN/Nb:STO interface is as illustrated in Fig. 3(A), which is consistent the previous reports on AlN growth on $SrTiO_3(111)$ single-crystal substrates, although Nb:STO is used in this study.[16)–18)] Therefore, Nb doping into STO negligibly affected the *in-plane* orientation relationship.

As shown in Fig. 3, the abundance of the two domains varies with the cation composition x. The fraction of the domain with the WZ-(Al,Sc)N[100]//Nb:STO[$1\bar{1}0$] relationship gradually increased with the concentration of Sc. A single-domain film with the WZ-(Al,Sc)N[100]// Nb:STO[$1\bar{1}0$] relationship was observed for $x > 0.3$. These characteristics are summarized in **Fig. 4**. $I_{(A)}$ and $I_{(B)}$ represent the integrated intensities of the domains with (Al,Sc)N[100]//Nb:STO[$11\bar{2}$] and (Al,Sc)N[100]// Nb:STO[$1\bar{1}0$], respectively. The fraction $I_{(B)}/(I_{(A)} + I_{(B)})$ increased from 20 to 100 % as the Sc content increased from 0 to 0.37, revealing change in a domain preference for Sc in WZ-$(Al_{1-x}Sc_x)N$. Considering that the fraction of the domain changed gradually with the chemical compo-

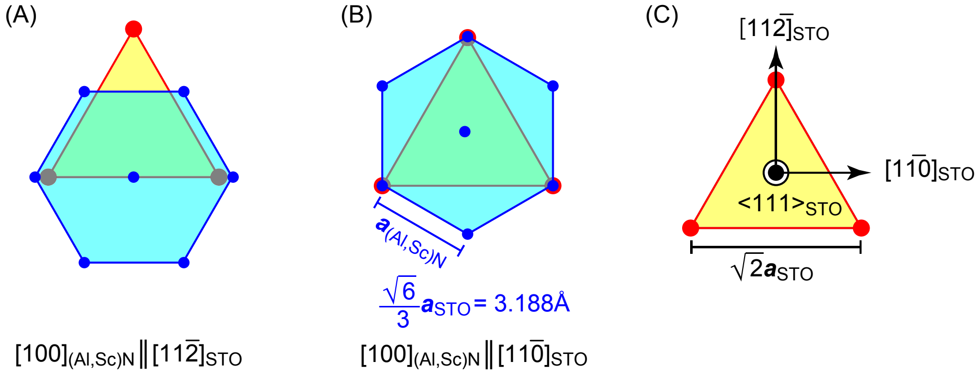

Fig. 3. Schematic of the epitaxial relationship between the (001) face of the $(Al_{1-x}Sc_x)N$ film and the (111) face of the Nb-doped $SrTiO_3$ substrate. Both (A) WZ-(Al,Sc)N[100]//Nb:STO[1$\bar{1}$0] and (B) WZ-(Al,Sc)N[100]// Nb:STO[11$\bar{2}$] relationships are illustrated with (C) the (111) face of the Nb-doped $SrTiO_3$ substrate. Here, the *in-plane* (*a*-axis) lattice parameter of the $(Al_{1-x}Sc_x)N$ film was assumed to be 3.188 Å, referring to the size of the oxygen sublattice on the (111) face of the Nb-doped $SrTiO_3$ substrate.

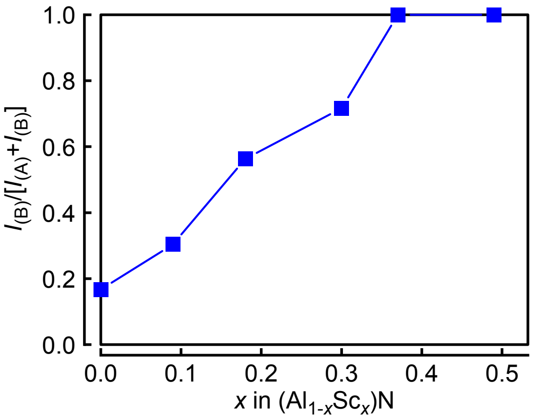

Fig. 4. Fraction of the rotation domains, WZ-(Al,Sc)N[100]// Nb:STO[11$\bar{2}$] ($I_{(A)}$) and WZ-(Al,Sc)N[100]//Nb:STO[1$\bar{1}$0] ($I_{(B)}$), deduced from the results of φ scan measurements for $(Al_{1-x}Sc_x)N$.

sition, the change in the interfacial structure was negligible. We assume that the presence of two domains results from a combination of several parameters. The change in the volume fraction of the domain by deposition temperature was reported.[17),18)] That study has shown that single domain films with (Al,Sc)N[100]//Nb:STO[11$\bar{2}$] were obtained at 270 and 370 °C and films with mixed domains were grown above 470 °C; namely, domain with (Al,Sc)N[100]//Nb:STO[1$\bar{1}$0] increases with the increase in deposition temperature.[17),18)] However, the domain with (Al,Sc)N[100]//Nb:STO[1$\bar{1}$0] was still minor in the films deposited at the highest temperature of 570 °C.[17),18)] By contrast, single domain with (Al,Sc)N[100]//Nb:STO[1$\bar{1}$0] was achieved by Sc addition with $x \geq 0.37$ in this study.

Figure 5 shows the composition dependence of the *c*-axis lattice constant (*c*) and *a*-axis lattice constant (*a*). For a hexagonal structure, *a* and *c* can be calculated from the *d*-spacing of the plane indexed by *h*, *k*, and *l* as follows:

$$\frac{1}{d^2_{(hkl)}} = \frac{4}{3}\frac{h^2+k^2+hk}{a^2} + \frac{l^2}{c^2} \qquad (1)$$

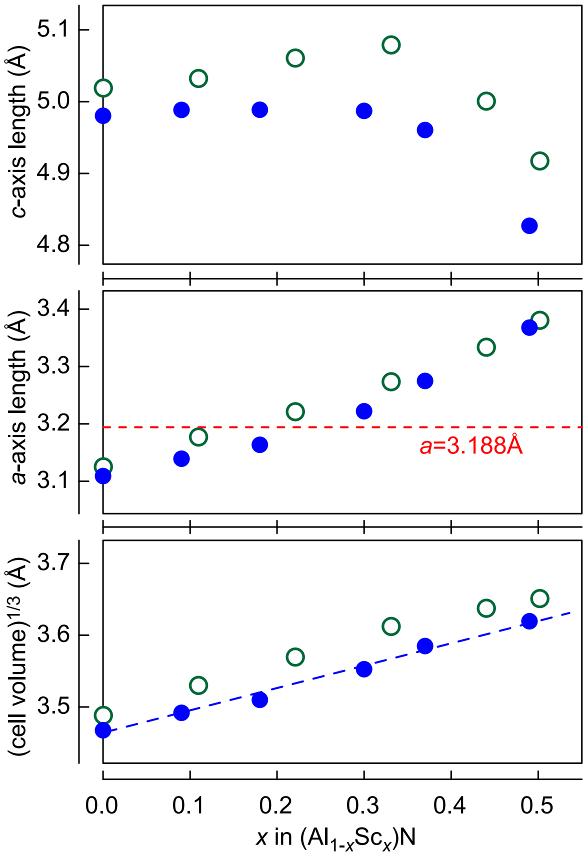

Fig. 5. Structural parameter of WZ-$(Al_{1-x}Sc_x)$ thin films with $0 \leq x < 0.5$. Blue closed circles indicate the experimental results of this study, and the open green circles indicate reported theoretical values.[9)] Dashed red line assumes the complete restriction of the *a*-axis parameter by the Nb-doped $SrTiO_3$ substrate with the (Al,Sc)N[100]//Nb:STO[1$\bar{1}$0] configuration. Dashed blue line is a visual guide.

In this study, we determined *c* from *out-of-plane* measurements of the 002 diffraction. We then determined *a* from the calculated *c* and the results of 101 diffraction measurements. As mentioned previously, the parameter *c* remained approximately unchanged for $0 \leq x \leq 0.3$ and decreased with increasing Sc content for $0.3 < x < 0.5$. This behavior is unconventional considering the ionic radii. The a parameter increased almost linearly with the Sc content, as expected from ionic radii of Al and Sc. The theoretical a and c values calculated by Furuta et al.[25] are also shown in Fig. 5. Notably, the change in the calculated lattice parameters with x also showed the two features observed in this study. A non-monotonic change in c-axis length, namely, a slight increase in value for $x \leq 0.3$ and a rapid decrease for $0.3 < x < 0.5$, was deduced from the calculated lattice parameters. Furthermore, a monotonic increase in a-axis length with increasing x was noted in both their simulations and our experimental results. Figure 5 plots the cubic root of the lattice volume, in order to validate solubility of scandium. The cubic root of the lattice volume exhibited an almost linear change with x, following the Vegard's law. This suggests that a WZ-(Al,Sc)N solid solution is obtained for all values of x in this study despite the abrupt change in the position of the XRD peaks shown in Fig. 2. Notably, Akiyama et al.[5] reported a steep decrease in the c-axis length with increasing Sc concentration for high x values in WZ-(Al$_{1-x}$Sc$_x$)N deposited on a platinum electrode. Hence, the x-dependence of the lattice parameters shown in Fig. 5 probably represents a general trend for any bottom electrode material.

Compared with the lattice parameter of Nb:STO, lattice mismatch does not strongly affect the epitaxial relationship. The lattice mismatch between WZ-(Al$_{1-x}$Sc$_x$)N ($x \approx 0.3$) and Nb:STO for the (Al,Sc)N[100]//Nb:STO[1$\bar{1}$0] relationship was small, as illustrated in Figs. 3 and 5. The nitrogen sublattice at WZ-(Al$_{1-x}$Sc$_x$)N(001) face should match the oxygen sublattice at the Nb:STO(111) face for a WZ-(Al$_{1-x}$Sc$_x$)N a-axis length of 3.188 Å under the (Al,Sc)N[100]//Nb:STO[1$\bar{1}$0] epitaxial relationship. However, the domain with the (Al,Sc)N[100]//Nb:STO[11$\bar{2}$] configuration is retained despite a large lattice mismatch of approximately 15 %. Therefore, other factors, including the adsorption energy[26] at the interface between WZ-(Al$_{1-x}$Sc$_x$)N(001) and Nb:STO(111), determine the epitaxial relationship. As previously mentioned, the *in-plane* lattice parameter changed monotonically with x, indicating that the WZ-(Al$_{1-x}$Sc$_x$)N lattice was well relaxed in the film prepared in this study.

4. Conclusions

WZ-(Al$_{1-x}$Sc$_x$)N thin films were epitaxially grown on Nb:STO(111) single-crystal substrates via RF reactive magnetron sputtering. c-axis-oriented WZ-(Al$_{1-x}$Sc$_x$)N thin films were obtained for $0 \leq x \leq 0.49$. The investigation of the epitaxial relationship revealed two coexisting domains, expressed as (Al,Sc)N[100]//Nb:STO[11$\bar{2}$] and (Al,Sc)N[100]//Nb:STO[1$\bar{1}$0]. Their relative abundance changed systematically with the cation composition. The domain with the (Al,Sc)N[100]//Nb:STO[11$\bar{2}$] configuration was dominant in the AlN film, and films with $x > 0.3$ had a single domain with the (Al,Sc)N[100]// Nb:STO[1$\bar{1}$0] configuration. These results imply that the lattice alignment of the WZ-(Al$_{1-x}$Sc$_x$)N thin films is not strongly restricted by the crystal structure of the Nb:STO substrate. The c-axis length was maximum at $x \approx 0.3$, whereas the a-axis length monotonically increased with an increase in x. Despite the non-monotonic change in the c-axis length with the chemical composition, the x-dependency of the unit cell volume showed that this solid-solution system follows the Vegard's law.

The crystal structure of the WZ-(Al$_{1-x}$Sc$_x$)N solid solution on the Nb:STO substrate is well relaxed and not strongly restricted by the substrate lattice. Considering that the c/a ratio of WZ-(Al$_{1-x}$Sc$_x$)N is an essential parameter for determining the ferroelectric behavior of this solid-solution system and that the restriction of c/a with the substrate lattice allows the control of their ferroelectric properties, further investigations of bottom electrode materials are required to achieve strain engineering and control the c/a ratio of this solid-solution system.

Acknowledgments Part of this study was performed at the Tokodai Institute for Elemental Strategy (TIES) and supported by the grant number JPMXP0112101001. This work was also supported by MEXT Program: Data Creation and Utilization Type Material Research and Development Project Grant Number JPMXP1122683430. This work was partly supported by JST and PRESTO under the grant number JPMJPR20B3.

References

1) R. Yu, G. Liu, G. Wang, C. Chen, M. Xu, H. Zhou, T. Wang, J. Yu, G. Zhao and L. Zhang, *J. Mater. Chem. C*, 9, 1852–1873 (2021).
2) Z. Valdez-Nava, D. Kenfaui, M. L. Locatelli, L. Laudebat and S. Guillemet, 2019 IEEE International Workshop on Integrated Power Packaging (IWIPP) (2019) pp. 91–96.
3) M. D. Williams, B. A. Griffin, T. N. Reagan, J. R. Underbrink and M. Sheplak, *J. Microelectromech. S.*, 21, 270–283 (2012).
4) H. Hirayama, N. Maeda, S. Fujikawa, S. Toyoda and N. Kamata, *Jpn. J. Appl. Phys.*, 53, 100209 (2014).
5) M. Akiyama, T. Kamohara, K. Kano, A. Teshigahara, Y. Takeuchi and N. Kawahara, *Adv. Mater.*, 21, 593–596 (2009).
6) Y. Song, C. Perez, G. Esteves, J. S. Lundh, C. B. Saltonstall, T. E. Beechem, J. I. Yang, K. Ferri, J. E. Brown, Z. Tang, J. P. Maria, D. W. Snyder, R. H. Olsson, III, B. A. Griffin, S. E. Trolier-McKinstry, B. M. Foley and S. Choi, *ACS Appl. Mater. Inter.*, 13, 19031–19041 (2021).
7) S. Fichtner, N. Wolff, F. Lofink, L. Kienle and B. Wagner, *J. Appl. Phys.*, 125, 114103 (2019).
8) T. Nakayama, Y. Nakano, A. Kamisawa and H. Takasu, *Jpn. J. Appl. Phys.*, 33, 5207–5210 (1994).
9) C. S. Hwang, B. T. Lee, C. S. Kang, J. W. Kim, K. H. Lee, H. J. Cho, H. Horii, W. D. Kim, S. I. Lee, Y. B. Roh and M. Y. Lee, *J. Appl. Phys.*, 83, 3703–3713 (1998).
10) T. Aoyama, S. Yamazaki and K. Imai, *Jpn. J. Appl. Phys.*, 39, 6348–6357 (2000).
11) R. Nie, S. Shao, Z. Luo, Z. Kang and T. Wu, *Micromachines-Basel*, 13, 1629 (2022).

12) K. Hasegawa, T. Shimizu and N. Ohashi, *J. Ceram. Soc. Jpn.*, 118, 921–926 (2022).
13) H. Moriwake, R. Yokoi, A. Taguchi, T. Ogawa, C. A. J. Fisher, A. Kuwabara, Y. Sato, T. Shimizu, Y. Hamasaki, H. Takashima and M. Itoh, *APL Mater.*, 8, 121102 (2020).
14) K. Yazawa, D. Drury, A. Zakutayev and G. L. Brennecka, *Appl. Phys. Lett.*, 118, 162903 (2021).
15) H. Fujioka, J. Ohta, H. Katada, T. Ikeda, Y. Noguchi and M. Oshima, *J. Cryst. Growth*, 229, 137–141 (2001).
16) J. Ohta, H. Fujioka, M. Kawano and M. Oshima, *Phys. Status Solidi C*, 0, 1 (2002).
17) Z. Q. Yao, X. Fan, B. He, W. J. Zhang, I. Bello, S. T. Lee and X. M. Meng, *Appl. Phys. Lett.*, 92, 241911 (2008).
18) Z. Q. Yao, X. Fan, B. He, W. J. Zhang, I. Bello, S. T. Lee and X. M. Meng, *Appl. Phys. Lett.*, 96, 109901 (2010).
19) C. Wang and M. Kryder, *J. Phys. D Appl. Phys.*, 41, 245301 (2008).
20) V. Nagarajan, I. G. Jenkins, S. P. Alpay, H. Li, S. Aggarwal, L. Salamanca-Riba, A. L. Roytburd and R. Ramesh, *J. Appl. Phys.*, 86, 595–602 (1999).
21) W. Li and M. Alexe, *Appl. Phys. Lett.*, 91, 262903 (2007).
22) T. Ohsawa, T. Murakami, T. Hosaka, S. Ueda, T. Ishigaki and N. Ohashi, *J. Phys. Chem. C*, 125, 14836–14842 (2021).
23) N. S. VanDamme, S. M. Richard and S. R. Winzer, *J. Am. Ceram. Soc.*, 72, 1409–1414 (1989).
24) R. D. Shanon, *Acta Crystallogr. A*, 32, 751–767 (1976).
25) K. Furuta, K. Hirata, S. A. Anggraini, M. Akiyama, M. Uehara and H. Yamada, *J. Appl. Phys.*, 130, 024104 (2021).
26) J. Wang, G. Tang, X. S. Wu and M. Gu, *J. Cryst. Growth*, 353, 134–139 (2012).